ACCSCIENCE PUBLISHING

Materials Science in Additive Manufacturing

ORIGINAL RESEARCH ARTICLE

Microstructural evolution and mechanical properties of laser-powder bed fusion-fabricated Ti-10Ta-2Nb-2Zr alloy as a potential orthopedic implant material

Igor Polozov*, Victoria Nefyodova, Anton Zolotarev, and Anatoly Popovich

Scientific and Educational Center, Structural and Functional Materials, Institute of Mechanical Engineering, Materials, and Transport, Peter the Great Saint Petersburg Polytechnic University, Saint Petersburg, Russia

(This article belongs to the *Special Issue: Advances in Tailoring of Microstructure, Materials, and Design with Additive Manufacturing*)

Abstract

Titanium alloys are gaining attention for their potential to improve implant performance in biomedical applications. This study investigates the Ti-10Ta-2Nb-2Zr alloy fabricated using laser-powder bed fusion (L-PBF) for potential biomedical applications. The research aims to examine the influence of processing parameters on material structure and properties, and to develop porous structures based on triply periodic minimal surfaces (TPMS) to reduce elastic modulus and improve mechanical compatibility with bone tissue. Spherical Ti-10Ta-2Nb-2Zr powder was processed using L-PBF with varying laser power (250 – 280 W), scanning speed (500 – 1000 mm/s), and hatch spacing (80 – 100 μm). Maximum relative density of 99.91% was achieved at volumetric energy density of 70 J/mm^3. Differential scanning calorimetry revealed the β-transus temperature at 862°C. Microstructural analysis showed the formation of martensitic α'-phase in the as-built condition with acicular morphology. Heat treatment at 900°C resulted in the formation of a lamellar α + β structure. Mechanical properties in the as-built condition were characterized by yield strength of 551.8 MPa, ultimate tensile strength of 641.2 MPa, elongation of 19.0%, and elastic modulus of 89.0 GPa. After heat treatment, strength characteristics decreased by 15 – 18%, whereas elastic modulus reduced to 86.0 GPa. TPMS porous structures (gyroid, Schwarz, and split) with 50% porosity demonstrated an elastic modulus of 9.2 – 9.7 GPa, representing approximately 18% of the solid material value. These results demonstrate the potential of Ti-10Ta-2Nb-2Zr as a promising alternative to conventional Ti-6Al-4V for orthopedic applications, offering enhanced mechanical properties and reduced stress shielding due to its lower elastic modulus and tailored porous architectures.

Keywords: Titanium alloy; Laser powder bed fusion; Biomaterials; Triply periodic minimal surfaces; Mechanical properties; Microstructure

***Corresponding author:**
Igor Polozov
(polozov_ia@spbstu.ru)

Citation: Polozov I, Nefyodova V, Zolotarev A, Popovich A. Microstructural evolution and mechanical properties of laser-powder bed fusion-fabricated Ti-10Ta-2Nb-2Zr alloy as a potential orthopedic implant material. *Mater Sci Add Manuf.* 2025;4(3):025220044. doi: 10.36922/MSAM025220044

Received: May 30, 2025

Revised: July 7, 2025

Accepted: July 9, 2025

Published online: August 12, 2025

1. Introduction

Titanium (Ti) and its alloys have gained widespread recognition as biomaterials due to their unique combination of high specific strength, excellent corrosion resistance, and superior biocompatibility.[1,2] However, the traditional Ti-6Al-4V alloy, which dominates biomedical applications, has two significant limitations: a relatively high elastic modulus (~110 – 120 GPa) compared to human bone tissue (10 – 30 GPa for cortical bone), and concerns regarding the potential long-term toxicity of aluminum (Al) and vanadium (V) ions released into surrounding tissues.[3,4] These limitations have stimulated extensive research efforts aimed at developing novel Ti alloys specifically designed for biomedical applications, with particular emphasis on reducing the elastic modulus to minimize stress shielding effects while maintaining adequate mechanical strength and biocompatibility.

Stress shielding represents a critical clinical problem in orthopedic implants, arising from a significant mismatch between the elastic moduli of the implant material and surrounding bone tissue. This mechanical incompatibility results in the stiffer implant bearing a greater portion of applied loads, leading to reduced mechanical stimulation of adjacent bone. Consequently, bone remodeling is disrupted, resulting in bone resorption, osteoporosis, and potential implant loosening over time.[4,5] The risk of stress shielding increases proportionally with the difference between implant and bone elastic moduli, making the development of low-modulus implants a paramount objective in orthopedic biomaterial research.

Beyond developing new alloys, researchers have paid significant attention to a structural approach for addressing elastic modulus mismatch through the application of lattice structures based on triply periodic minimal surfaces (TPMS).[6] These biomimetic structures enable a significant reduction in the effective elastic modulus of implants to values comparable to those of bone tissue, regardless of the base material.[7] A key advantage of TPMS structures is the ability to control mechanical properties through variation of parameters such as relative density, unit cell type (gyroid, Schwarz, split, etc.), and their geometric characteristics. Moreover, the porous architecture of lattice structures promotes enhanced osteointegration by providing optimal pore sizes for bone tissue ingrowth and efficient nutrient transport.[8,9]

Beta-Ti alloys have emerged as promising candidates for addressing these issues due to their inherently lower elastic modulus compared to α and α + β Ti alloys. The β-phase has a body-centered cubic (BCC) crystal structure, which fundamentally exhibits lower stiffness than the hexagonal close-packed (HCP) structure of the α-phase.[10] This characteristic makes β-Ti alloys particularly attractive for load-bearing orthopedic applications where modulus matching with bone tissue is critical. Recent advances in β-Ti alloys have enabled the development of compositions with elastic moduli as low as 40 – 80 GPa, which is substantially closer to natural bone properties compared to traditional implant alloys.[11,12]

Several β-stabilizing elements, including niobium (Nb), tantalum (Ta), molybdenum (Mo), and zirconium (Zr), have been thoroughly investigated for biomedical Ti alloys due to their superior biocompatibility and ability to reduce elastic modulus while maintaining adequate mechanical strength.[13] Among these elements, Ta has attracted significant attention due to its exceptional biocompatibility, outstanding corrosion resistance, and strong tendency to stabilize the β-phase in Ti.[14-16] When alloyed with Ti, even at relatively modest concentrations, Ta promotes the formation of the BCC crystal structure, which exhibits a lower elastic modulus than the HCP structure of pure Ti or predominantly α-alloys.

Notable developments in this field include the Ti-Nb alloy family, with compositions such as Ti-35Nb-7Zr-5Ta demonstrating promising combinations of low elastic modulus and good biocompatibility.[17,18] Similarly, Ti-24Nb-4Zr-8Sn has shown excellent superelasticity with an elastic modulus of only 53 GPa.[19] Other β-alloys, such as Ti-29Nb-13Ta-4.6Zr and Ti-35Nb-5Ta-7Zr, have also demonstrated favorable combinations of mechanical properties and biocompatibility for orthopedic implants.[20,21] However, many of these compositions contain relatively high concentrations of expensive elements, such as Nb and Ta, potentially limiting their widespread clinical application.

Binary Ti-Ta alloys, particularly those containing 20 – 40 wt.% of Ta, have demonstrated promising combinations of relatively low elastic modulus (65 – 70 GPa) and good biocompatibility.[22] However, these binary alloys often suffer from processing issues due to the high melting point of Ta (3,017°C) and its significant density difference compared to Ti. In addition, the high cost of Ta makes high-Ta content alloys economically less attractive for widespread clinical application. To address these limitations while retaining the beneficial properties of Ta, the development of multi-component Ti-Ta alloys with reduced Ta content and the addition of other β-stabilizing elements has attracted attention.[23,24]

The Ti-10Ta-2Nb-2Zr alloy represents a strategic design approach that utilizes synergistic effects between different alloying elements.[25] Ta provides primary β-stabilization and biocompatibility, while Nb contributes additional β-stabilization and may enhance mechanical properties through solid solution strengthening. Zr, as a

neutral alloying element, can improve strength without significantly affecting phase stability and has been reported to enhance the corrosion resistance of Ti alloys. The reduced Ta content (10 wt.%) offers substantial economic advantages compared to higher Ta content alloys while potentially retaining most of the beneficial properties associated with Ta addition. The significance of this alloy lies in its elimination of potentially toxic elements (Al, V) present in conventional Ti-6Al-4V, making it more suitable for long-term biomedical applications. Furthermore, the combination of optimized chemical composition with advanced manufacturing techniques, such as laser powder bed fusion (L-PBF), enables the development of complex porous architectures that can achieve elastic modulus values approaching those of natural bone tissue. This dual approach of compositional design and structural engineering represents a promising strategy for next-generation orthopedic implants with enhanced mechanical compatibility.

Traditional manufacturing methods for Ti-Ta alloys include casting, forging, and powder metallurgy approaches, each presenting specific challenges in utilizing Ta due to its high melting point, segregation issues, and difficulties in achieving homogeneous microstructures.[26,27] L-PBF, an additive manufacturing method, offers distinct advantages for processing these alloys, including the ability to create complex, patient-specific geometries, reduced material waste, and potentially improved microstructural control through rapid solidification conditions.[14,16] However, processing Ti-Ta-based alloys using L-PBF introduces challenges, including the need to optimize processing parameters to achieve high density, desired microstructures, and stable mechanical properties.

Previous studies of L-PBF Ti alloys containing Ta and other β-stabilizers have demonstrated the feasibility of achieving high-density components with promising mechanical properties. However, the influence of specific L-PBF processing parameters on densification behavior, microstructural evolution, and mechanical properties of the Ti-10Ta-2Nb-2Zr alloy has not been systematically investigated. Furthermore, the effect of thermal treatments on phase transformations, microstructural stabilization, and mechanical behavior of this alloy remains largely unexplored.

The present study aims to address these research gaps by:

(i) Systematically investigating the influence of L-PBF processing parameters on density, microstructure, and mechanical properties of the Ti-10Ta-2Nb-2Zr alloy;
(ii) Studying phase transformation behavior and microstructural evolution during thermal treatments;
(iii) Establishing correlations between processing parameters, microstructural features, and resulting mechanical properties, particularly regarding elastic modulus reduction, which is critical for biomedical applications;
(iv) Determining optimal processing windows and thermal treatment regimes to achieve the best combination of properties for orthopedic implants;
(v) Designing and evaluating the influence of TPMS lattice structures made from Ti-10Ta-2Nb-2Zr alloy on mechanical properties.

Through this comprehensive investigation, we aim to advance the understanding of process–structure–property relationships in this promising biomedical alloy and contribute to the development of improved Ti implants with enhanced biomechanical compatibility.

2. Materials and methods

2.1. Starting materials

The primary material used in this investigation was pre-alloyed Ti-10Ta-2Nb-2Zr powder (Guangzhou Sailong Additive Manufacturing Co., Ltd., China). The powder particles exhibited predominantly spherical morphology with satellite particles occasionally present on larger spheres (Figure 1A). Particle size distribution analysis performed using a laser analyzer (Fritsch Analysette 22, NanoTec plus, Germany) showed a size distribution with d_{10} = 11.3 μm, d_{50} = 29.1 μm, and d_{90} = 61.7 μm (Figure 1B).

Scanning electron microscopy (SEM) examination of the powder particles revealed surface morphology characterized by fine dendritic structures typical of rapid solidification during gas atomization (Figure 1C). Cross-sectional analysis combined with energy-dispersive X-ray spectroscopy (EDS) mapping confirmed uniform distribution of Ti, Ta, Nb, and Zr elements within individual particles, demonstrating good compositional homogeneity (Figure 1D). Chemical analysis of the powder showed the following composition (wt.%): Ti: Balance; Ta: 9.85 ± 0.18%; Nb: 1.95 ± 0.12%; Zr: 1.92 ± 0.10%.

2.2. L-PBF

Samples were fabricated using an L-PBF system (MINI, 3DLAM, Russia) equipped with a fiber laser IPG Photonics, USA) with a maximum power of 300 W and a beam diameter of 70 μm. Processing was conducted in a high-purity argon atmosphere (O_2 < 100 ppm) on a Ti build platform without pre-heating. The building strategy featured a linear scanning pattern with 90° rotation between consecutive layers for bulk volumes.

The selection of processing parameters was based on our previous experience with similar Ti alloys, where

high-density components were successfully manufactured within similar parameter ranges (Table 1). The processing parameters were systematically varied to investigate their influence on densification behavior and microstructural evolution. The volumetric energy density (E) was calculated using Equation I.

$$E = \frac{P}{V \cdot h \cdot t} \quad (I)$$

where P is laser power (W); V is scanning speed (mm/s); h is hatch spacing (μm); and t is layer thickness (μm).

Cubic samples (10 × 10 × 10 mm^3) were fabricated for density measurements and microstructural characterization. For mechanical testing, cylindrical tensile specimens were produced according to the American Society for Testing and Materials (ASTM) E8/E8M standard with a gauge length of 15 mm and a diameter of 3 mm.

2.3. Heat treatments

The selected specimens were heat-treated using the following parameters: vacuum annealing at 900°C for 1 h, followed by furnace cooling. The samples were heated at a rate of 10°C/min to the target temperature in a vacuum furnace (Carbolite Gero, UK) at a vacuum level of 10^{-5} mbar.

The selection of heat treatment temperature was based on differential scanning calorimetry (DSC) analysis, which identified the β-transus temperature range for the Ti-10Ta-2Nb-2Zr alloy. The annealing temperature of 900°C was

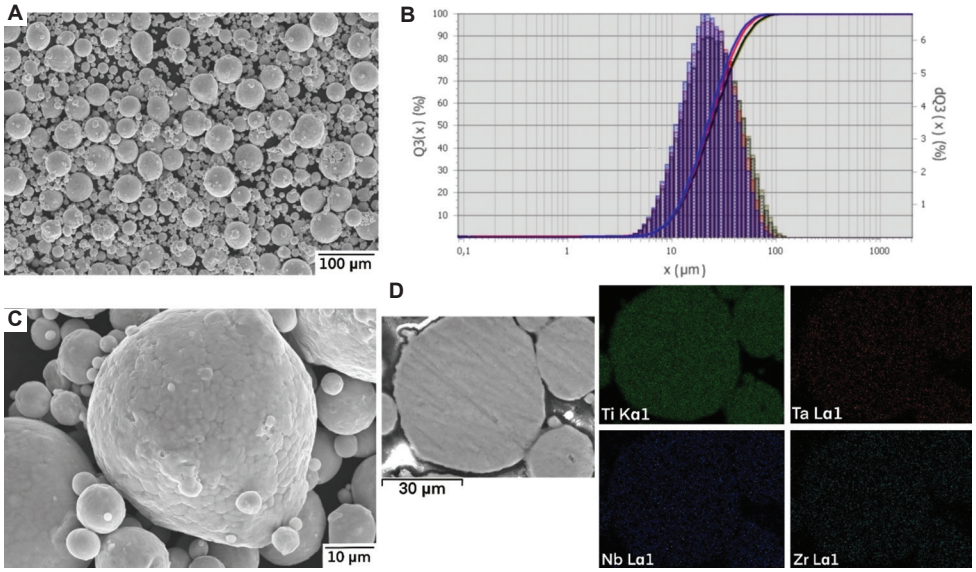

Figure 1. Characterization of Ti-10Ta-2Nb-2Zr powder. (A) Scanning electron micrograph shows general morphology of powder particles, scale bar: 100 μm; magnification: ×150; (B) Particle size distribution histogram with cumulative curve; (C) High-magnification SEM image of individual particle surface morphology, scale bar: 10 μm; magnification: ×1000; (D) cross-sectional scanning electron microscopic image with corresponding energy-dispersive X-ray spectroscopy mapping showing uniform Ti, Ta, Nb and Zr distribution, scale bar: 30 μm; magnification: ×1000

Table 1. Processing parameters used for laser-powder bed fusion of Ti-10Ta-2Nb-2Zr alloy

Regime	Power (P), W	Scanning speed (V), mm/s	Layer thickness (t), μm	Hatch spacing (h), μm	Energy density, J/mm^3
1	250	800	50	100	62.5
2	280	500	50	100	112.0
3	280	800	50	100	70.0
4	250	600	50	100	83.3
5	250	1,000	50	100	50.0
6	280	600	50	100	93.3
7	280	600	50	80	116.7
8	250	800	50	80	78.1
9	280	800	50	80	87.5

chosen to ensure complete transformation to the β-phase field, as it is approximately 40°C above the measured β-transus finish temperature (862°C). This temperature was selected to promote full recrystallization of the as-built microstructure while minimizing grain growth. Furnace cooling was selected to promote the formation of a stable lamellar α + β microstructure, balancing strength and ductility, which is critical for load-bearing orthopedic implants.

2.4. TPMS structures

As part of the investigation into the effects of cellular structures on the mechanical properties of alloys, experimental samples with three different TPMS architecture types were designed and fabricated: Schwarz, gyroid, and split (Figure 2). Computer-aided design of the TPMS architectures was performed using nTopology software (Version 3.0, nTopology Inc., USA). To ensure an optimal balance between mechanical characteristics and L-PBF manufacturing capabilities, a unit cell size of 1.5 mm was established for all architecture types. Adjustment of the wall thickness was performed to achieve the target volumetric porosity of 50%. For mechanical compression testing, cylindrical specimens with TPMS architecture were constructed with dimensions of 6 mm in diameter and 12 mm in height. During manufacturing, the samples were positioned so that the longitudinal axis of the cylinder aligned with the build direction.

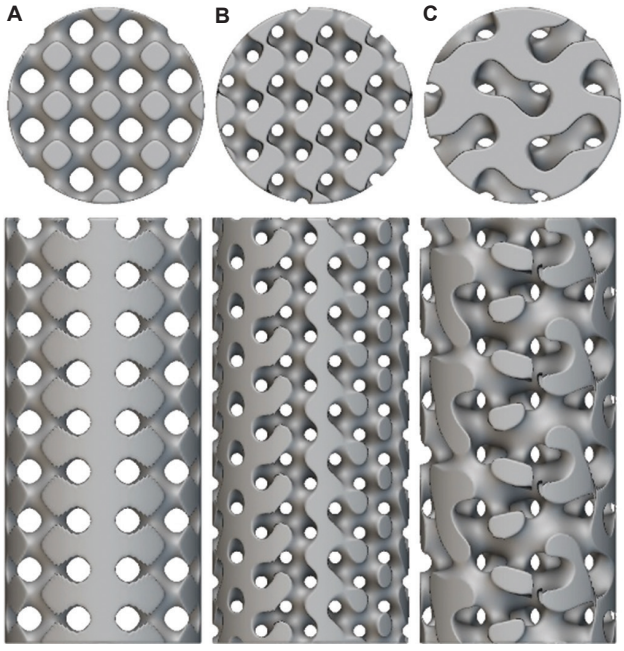

Figure 2. Designs of triply periodic minimal surface samples. (A) Schwarz; (B) gyroid; (C) split

The design of TPMS architectures took into consideration the technological limitations and capabilities of the L-PBF process. The sample dimensions were selected according to the work of Soro *et al.*,[28] whereas the unit cell size was adapted to account for the technical specifications of the printer used. The chosen parameters ensure that key structural elements comply with the minimum permissible dimensions for our L-PBF equipment while maintaining the required mechanical properties. The selected TPMS architecture types (Schwarz, gyroid, and split) represent designs whose feasibility in L-PBF processes has been confirmed by previous studies.[29,30] Nevertheless, the geometric features of these structures lead to variations in manufacturing accuracy. Among the considered variants, the split structure, characterized by the smallest constructive elements, demonstrates an increased susceptibility to manufacturing imperfections compared to gyroid and Schwarz structures, which is reflected in the variability of mechanical properties. To ensure uniformity in production conditions and resulting mechanical characteristics, all experimental samples were manufactured with the longitudinal axis of the cylinder oriented along the build direction. The positioning strategy and technological parameters were optimized based on published data on the successful fabrication of TPMS structures from Ti alloys. In addition, an investigation of the printed gyroid lattice structure was conducted to evaluate the influence of lattice geometry on the resulting microstructure, which established a relationship between the topological features of the cellular construction and microstructural parameters in various regions of the Ti-10Ta-2Nb-2Zr alloy specimen.

2.5. Characterization methods

2.5.1. Density analysis

The density of the fabricated samples was measured using the Archimedes method (hydrostatic weighing) with an analytical balance (XS205, Mettler Toledo, Switzerland) equipped with a density measurement kit. Distilled water was used as the immersion medium, and measurements were conducted at 22 ± 0.5°C. Four measurements were taken for each sample to ensure statistical reliability.

The theoretical density of the Ti-10Ta-2Nb-2Zr alloy was calculated using thermodynamic calculations in JMatPro 11 software (11.0, Sente Software Ltd., United Kingdom), which provides accurate density predictions based on the chemical composition and phase equilibria of the alloy system.

The relative density was determined as the ratio of the measured density (obtained using Archimedes' method) to the theoretical density (calculated using JMatPro 11).

2.5.2. Microstructural analysis

Samples for microstructural analysis were prepared using standard metallographic procedures. After grinding and polishing as described above, the specimens were etched using Kroll's reagent (2 mL HF, 6 mL HNO_3, and 92 mL H_2O) for 15 – 20 s at room temperature to reveal microstructural features.

Microstructural examination was performed using a SEM (MIRA 3, TESCAN, Czech Republic) equipped with an EDS detector for compositional analysis. Imaging was conducted at accelerating voltages between 15 and 20 kV using secondary electron and backscattered electron detectors to optimize contrast between different phases.

Phase analysis was performed using an X-ray diffractometer (D8 Advance, Bruker, Germany) with CuK-α radiation (λ = 1.5418 Å) operated at 40 kV and 40 mA. X-ray diffraction (XRD) patterns were recorded in the 2θ range of 30 – 90° with a step size of 0.02° and a counting time of 2 s per step. Phase identification was performed using the International Centre of Diffraction Data PDF-4 + database.

2.5.3. Mechanical testing

Vickers microhardness measurements were conducted using a hardness tester (Wilson VH1202, Buehler, USA) under a load of 500 g ($HV_{0.5}$) with a dwell time of 15 s. At least 10 indentations were made on each sample to ensure statistical significance, with indentation sites selected to avoid proximity to pores or sample edges.

Tensile tests were conducted on a universal testing machine (Zwick/Roell Z100, ZwickRoell GmbH & Co., Germany) at room temperature with a strain rate of 0.001 s^{-1} according to ASTM E8/E8M standard. A minimum of five specimens were tested for each processing condition to ensure reproducibility. The elastic modulus was determined using an extensometer attached to the gauge section during initial loading.

2.5.4. Thermal analysis

DSC was carried out using a simultaneous thermal analyzer (STA409, Netzch-Gerätebau GmbH, Germany) at a heating rate of 10°C/min under high-purity argon flow (50 mL/min). Samples with a mass of approximately 50 mg were placed in alumina crucibles and subjected to heating/cooling cycles between room temperature and 1,000°C to investigate phase transformation behavior. The temperature and heat flow calibrations were performed using high-purity standards before the measurements.

3. Results and discussion

3.1. Effect of L-PBF parameters on the relative density of Ti-10Ta-2Nb-2Zr alloy

Table 2 presents the density values obtained using the hydrostatic weighing method. The theoretical density of Ti-10Ta-2Nb-2Zr alloy calculated using JMatPro 11 thermodynamic software was 4.9400 g/cm³. Hydrostatic weighing revealed absolute density values ranging from 4.9153 to 4.9355 g/cm³, with the highest value of 4.9355 ± 0.0015 g/cm³ achieved at energy densities of 70 J/mm³ (laser power P = 280 W, scanning speed V = 800 mm/s).

The lowest relative density of 99.49 ± 0.21% was recorded at an energy density of 116.7 J/mm³ (P = 280 W, V = 600 mm/s, h = 50 μm), which may indicate the formation of keyhole porosity defects due to excessive energy input, consistent with findings for similar Ti-based alloys.[31] At the minimum energy density of 50.0 J/mm³ (P = 250 W, V = 1000 mm/s, h = 50 μm), the relative density reached 4.9212 ± 0.0054, demonstrating sufficient material melting.

The dependence of relative density on volumetric energy density (Figure 3) demonstrates a non-monotonic behavior. The highest density values were achieved in the range of 60 – 90 J/mm³, with a peak value of 99.91% at 70 J/mm³. Lower energy densities (<60 J/mm³) resulted in insufficient melting and increased porosity, while excessive energy input (>90 J/mm³) led to the formation of keyhole defects. The optimal energy density window appears to be broader than typically reported for binary Ti-Ta alloys,[14,16] suggesting enhanced processability of the quaternary composition.

These results underscore the importance of optimizing L-PBF parameters to achieve near-full densification (>99.85%) for biomedical implants, where high density

Table 2. Densities of the samples obtained using the hydrostatic weighing method and metallographic analysis

Regime	Measured density (g/cm³)	Relative density (%)
1	4.9326±0.0040	99.85±0.08
2	4.9153±0.0084	99.54±0.17
3	4.9355±0.0015	99.91±0.03
4	4.9192±0.0069	99.58±0.14
5	4.9212±0.0054	99.62±0.11
6	4.9282±0.0030	99.72±0.06
7	4.9153±0.0094	99.46±0.19
8	4.9207±0.0044	99.61±0.09
9	4.9242±0.0074	99.64±0.15

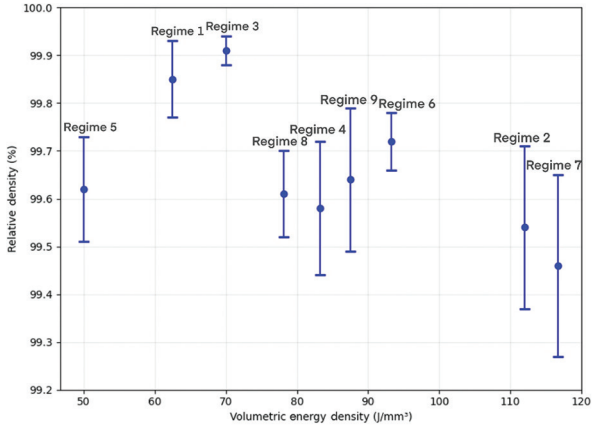

Figure 3. The influence of volumetric energy density on the relative density of the Ti-10Ta-2Nb-2Zr alloy

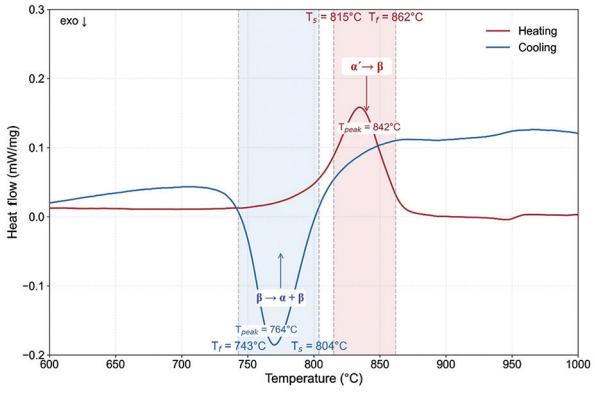

Figure 4. Differential scanning calorimetry curves of the Ti-10Ta-2Nb-2Zr alloy show phase transformations during heating and cooling at 20 K/min. The heating curve (red) exhibits an endothermic peak corresponding to α' → β transformation (T_s = 815°C, T_{peak} = 842°C, T_f = 862°C), while the cooling curve (blue) shows an exothermic peak associated with β → α + β transformation (T_s = 804°C, T_{peak} = 764°C, T_f = 743°C). Shaded regions indicate the temperature ranges of phase transformations

ensures mechanical integrity and corrosion resistance in physiological environments.[32] The composition of Ti-10Ta-2Nb-2Zr alloy that is free of toxic elements, such as Al and V, combined with its low elastic modulus (~75 GPa), based on similar β-stabilized alloys,[33] positions it as a promising alternative to Ti-6Al-4V for long-term implantation. The identified processing window (p=250 – 280 W, V = 600 – 800 mm/s, h = 80 – 100 μm, E = 62.5 – 83.3 J/mm^3) provides a robust foundation for fabricating defect-free, biocompatible implants with complex geometries.

3.2. DSC analysis

The thermal behavior of the Ti-10Ta-2Nb-2Zr alloy was investigated using DSC during heating and cooling cycles at a rate of 10 K/min, covering a temperature range from 600°C to 1,000°C. This analysis was performed to determine the β-transus temperature and understand phase transformation behavior, which is essential for optimizing heat treatment parameters and predicting microstructural evolution during thermal processing.

The DSC curves (Figure 4) reveal distinct phase transformation events characteristic of Ti alloys with β-stabilizing elements (Ta and Nb) and α-stabilizing elements (Zr). It should be noted that the as-built condition after L-PBF processing contains metastable α'-phase (martensite) due to the rapid cooling rates inherent in the additive manufacturing process, as confirmed by subsequent microstructural and XRD analyses (sections 3.3.1 and 3.3.3).

During heating, an endothermic peak at 842°C, with a starting temperature T_s of 815°C and a finishing temperature T_f of 862°C, indicates the α' → β phase transformation, where the metastable martensitic structure transforms into a single β-phase structure.[34] The exothermic nature of the cooling curve, with a peak at 764°C and boundaries at T_s = 804°C and T_f = 743°C, corresponds to the equilibrium β → α + β transformation, reflecting the precipitation of the α-phase within the β matrix under controlled cooling conditions.[13] These transformations are typical for near-β or β-Ti alloys and are influenced by the alloy composition and cooling rate.[35]

The observed phase transformation temperatures and their thermal signatures align with the expected behavior of Ti-based alloys with Ta, Nb, and Zr additions, which enhance β-phase stability and lower the martensitic transformation temperatures compared to pure Ti.[36] The hysteresis between heating and cooling curves (approximately 40 – 50°C) suggests a diffusion-controlled transformation mechanism during the equilibrium cooling process, which is common in Ti alloys under similar thermal conditions.[37]

These findings provide critical insights into the thermal stability and phase evolution of Ti-10Ta-2Nb-2Zr, enabling the optimization of heat treatment protocols to achieve desired microstructural and mechanical properties for biomedical applications.[38]

3.3. Microstructural analysis of as-built Ti-10Ta-2Nb-2Zr alloy

3.3.1. General microstructural features

The microstructure of as-built Ti-10Ta-2Nb-2Zr samples produced via L-PBF was characterized to understand the correlation between processing conditions and resulting material properties. Figure 5 presents SEM micrographs of the as-built microstructure at different magnifications.

The microstructure of the Ti-10Ta-2Nb-2Zr alloy fabricated with L-PBF is characterized by a pronounced acicular morphology. In Figure 5A, fine needle-like features are observed, organized into groups with predominantly parallel orientation. The needles intersect at angles of approximately 60 – 120°, forming a characteristic pattern of martensitic transformation.

At higher magnification Figure 5B, the morphology reveals more detail. The structure consists of needles 50 – 400 nm in width, densely packed with varying orientations. A high degree of structural refinement is observed, with no presence of large grains.

The acicular morphology with characteristic crystallographic relationships indicates the dominance of the α' martensitic phase. The presence of α' martensite is also possible.[14] The fine acicular α'-martensitic structure observed in the as-built condition is a direct result of the high cooling rates (10^5 – 10^6 K/s) inherent to the L-PBF process. These rapid cooling rates suppress diffusional transformations, stabilizing the metastable martensitic phase and contributing to the high strength of the alloy in the as-built state, which is advantageous for load-bearing applications.

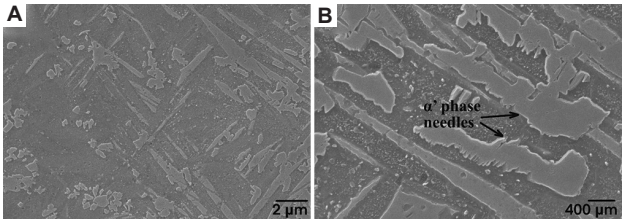

Figure 5. Scanning electron micrographs of as-built Ti-10Ta-2Nb-2Zr alloy. (A) Microstructure with intersecting needle-like features, characteristic of martensitic transformation, scale bar: 2 µm; magnification: ×5000; (B) High-magnification image showing densely packed needles with varied orientations and refined structure, scale bar: 400 nm; magnification: ×20000

3.3.2. Elemental distribution analysis

Elemental mapping using EDX was performed to evaluate the distribution of alloying elements within the as-built microstructure. Figure 6A presents an SEM micrograph of the analyzed region, whereas Figure 6B-E shows the corresponding elemental maps for Ti, Ta, Nb, and Zr, respectively.

The EDX mapping reveals a remarkably uniform distribution of all alloying elements throughout the microstructure, despite the rapid solidification conditions of the L-PBF process. Ti, as the matrix element, shows high and consistent concentration across the entire mapped area (Figure 6B). Notably, Ta (Figure 6C), Nb (Figure 6D), and Zr (Figure 6E) exhibit homogeneous distributions without significant segregation or clustering, which is particularly remarkable considering the high melting point of Ta (3,017°C) and its significant density difference compared to Ti.

This chemical homogeneity can be attributed to several factors: the pre-alloyed powder composition that provides a uniform starting distribution of elements; complete melting achieved with the selected laser parameters; the restricted time available for element diffusion and segregation during rapid solidification; and potential multiple remelting of preceding layers during the layer-by-layer building process.

3.3.3. Phase composition analysis

XRD analysis was conducted to identify the phase composition of the Ti-10Ta-2Nb-2Zr alloy in the as-built and heat-treated conditions. Figure 7 presents the XRD

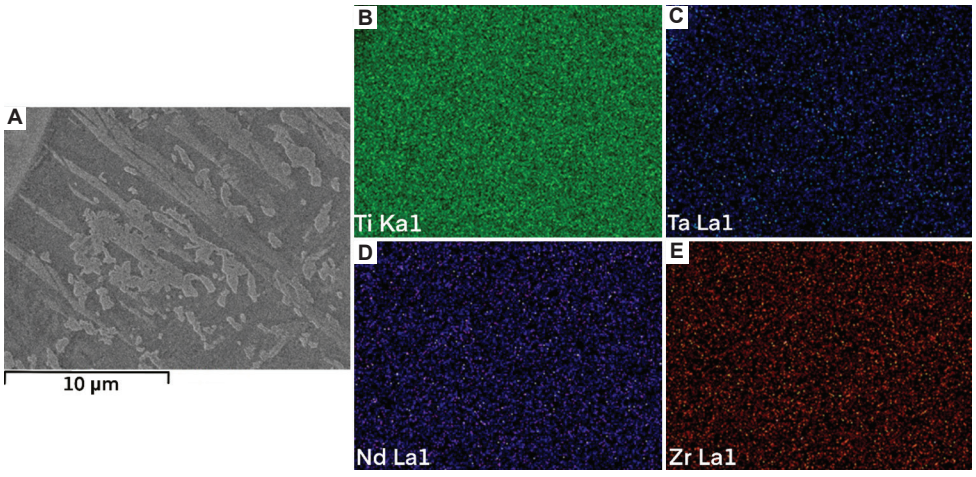

Figure 6. Elemental distribution in as-built Ti-10Ta-2Nb-2Zr alloy. (A) Scanning electron micrograph of analyzed region, scale bar: 10 µm; magnification: ×4000; elemental distribution maps of (B) Titanium; (C) Tantalum; (D) Niobium; (E) Zirconium

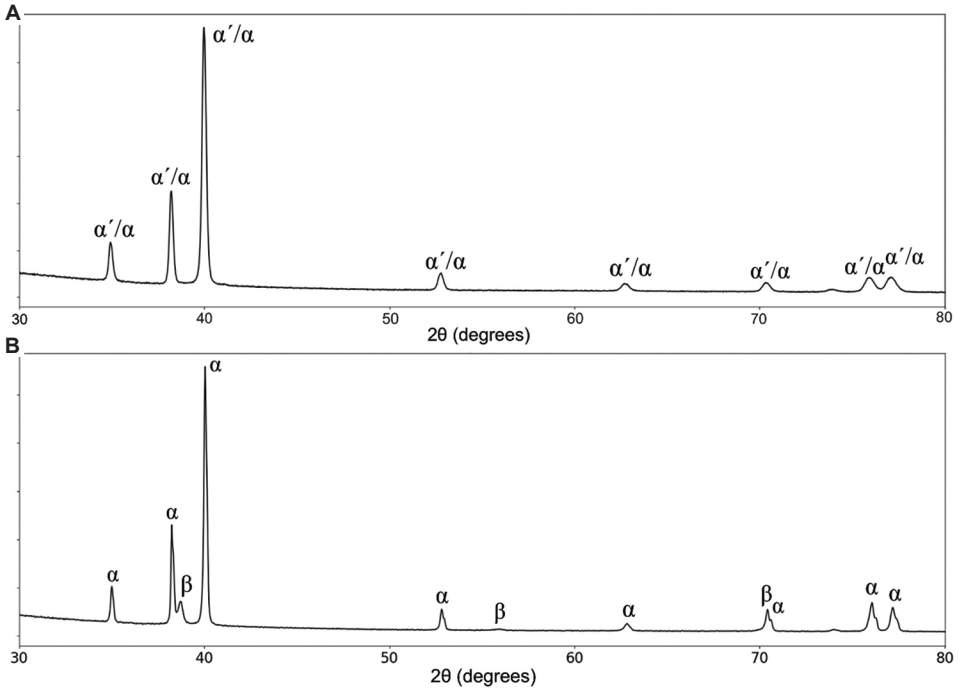

Figure 7. X-ray diffraction patterns of the Ti-10Ta-2Nb-2Zr alloy. (A) As-built condition; (B) After heat treatment

patterns obtained from the samples: Figure 7A corresponds to the as-built condition, while Figure 7B shows the results after heat treatment.

The XRD pattern reveals that the as-built microstructure consists predominantly of α' martensitic phase with HCP crystal structure. The most intense diffraction peak appears at approximately 40° (2θ), corresponding to the α-Ti (101) plane. Other characteristic α-Ti reflections are observed at approximately 35° (100), 38° (002), 53°, 63°, 70°, and 76 – 77° (doublet). The peaks exhibit some broadening, indicative of high levels of internal stress and small crystallite size typical of rapid solidification during L-PBF.

No distinct peaks associated with β-phase BCC are visible in the pattern, suggesting that the high cooling rates during L-PBF processing promoted almost complete transformation to α' martensite. The slight shifts in peak positions compared to pure Ti result from lattice distortion caused by the incorporation of alloying elements (Ta, Nb, Zr).

These XRD results align with the SEM observations of acicular microstructure characteristic of martensitic transformation. The dominant martensitic structure is consistent with the phase transformation behavior identified in the DSC analysis (Section 3.2), where the $\beta \rightarrow \alpha + \beta$ transformation during cooling was detected in the temperature range of 804 – 743°C. During L-PBF processing, the cooling rates far exceed those used in DSC analysis, further promoting the formation of a non-equilibrium martensitic phase instead of the equilibrium $\alpha + \beta$ structure.

3.4. Mechanical properties of Ti-10Ta-2Nb-2Zr alloy

3.4.1. Tensile properties

The tensile properties of the Ti-10Ta-2Nb-2Zr alloy in the as-built condition and after heat treatment are summarized in Table 3. Each value represents the average of multiple specimens, with standard deviations provided to indicate the variability of the measurements.

The as-built Ti-10Ta-2Nb-2Zr specimens exhibited high strength characteristics of a yield strength of 551.8 ± 8.4 MPa and an ultimate tensile strength of 641.2 ± 5.7 MPa, combined with a good ductility indicated by an elongation of 19.0 ± 1.8% and a reduction in area of 58.0 ± 2.3%. The elastic modulus in the as-built condition was 89.0 ± 2.4 GPa, which is significantly lower than that typically reported for conventional Ti alloys such as Ti-6Al-4V (110 – 120 GPa).

The application of heat treatment (vacuum annealing at 900°C for 1 h) resulted in a notable decrease in strength properties (Figure 8), with the yield strength reduced by 18.0% – 452.3 ± 14.7 MPa and the ultimate tensile strength reduced by 15.0% – 545.0 ± 3.6 MPa. Interestingly, the elongation slightly increased to 20.2 ± 3.6%, while the

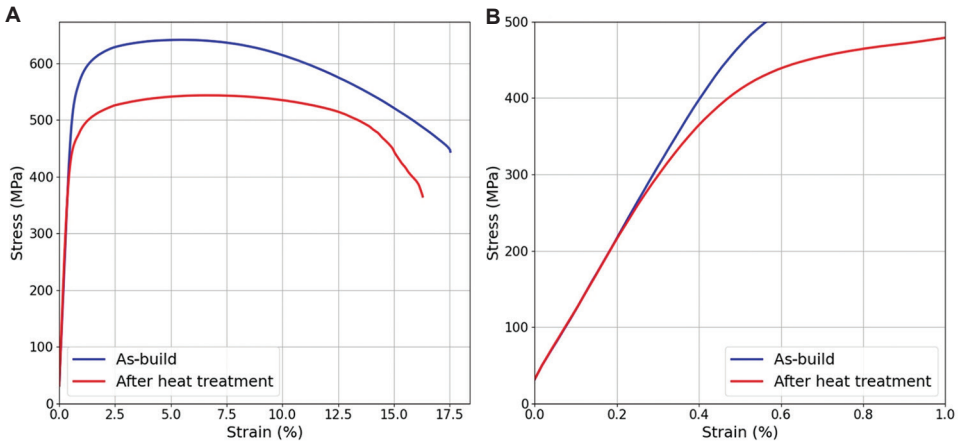

Figure 8. Comparison of strength properties between as-built and annealed Ti-10Ta-2Nb-2Zr. (A) Representative engineering stress-strain curves for Ti-10Ta-2Nb-2Zr alloy in as-built condition and after heat treatment; (B) Enlarged view of the elastic region

Table 3. Tensile properties of Ti-10Ta-2Nb-2Zr alloy and their comparison with other biomedical alloys in different conditions

Alloy condition	Elastic modulus (GPa)	Yield strength (MPa)	Tensile strength (MPa)	Elongation (%)	Reduction in area (%)	References
Ti-10Ta-2Nb-2Zr, as-built	89.0±2.4	551.8±8.4	641.2±5.7	19.0±1.8	58.0±2.3	Current study
Ti-10Ta-2Nb-2Zr, after annealing	86.0±2.2	452.3±14.7	545.0±3.6	20.2±3.6	45.8±15.5	Current study
Ti-6Al-4V	110 – 120	-	~900 – 1000	~10 – 15%	-	39,40
Ti-35Nb-7Zr-5Ta	81	-	630	15	-	18

reduction in area decreased to 45.8 ± 15.5%. The elastic modulus after annealing decreased to approximately 86.0 GPa, representing a 3.4% reduction compared to the as-built condition.

3.4.2. Microhardness measurements

Microhardness measurements were performed on samples fabricated using different L-PBF processing regimes. The results are presented in Table 4.

The microhardness of the Ti-10Ta-2Nb-2Zr alloy exhibited relatively consistent values across different L-PBF processing regimes, with an average of 224 $HV_{0.5}$ and standard deviations within a narrow range. The variation in hardness values did not show a strong correlation with processing parameters, indicating that the mechanical properties of the alloy remain stable across the investigated processing window. The highest hardness value of 231 $HV_{0.5}$ was observed in Regime 7 (with the highest energy density of 116.7 J/mm^3), while the lowest hardness value of 216 $HV_{0.5}$ was measured in Regime 3. This relatively narrow range of hardness values (216 – 231 $HV_{0.5}$) suggests good process stability for the Ti-10Ta-2Nb-2Zr alloy during L-PBF manufacturing.

Table 4. Microhardness of Ti-10Ta-2Nb-2Zr alloy fabricated using different L-PBF processing regimes

Regime	Energy density (J/mm^3)	Microhardness ($HV_{0.5}$)
1	62.5	227±7
2	112.0	222±4
3	70.0	216±6
4	83.3	225±7
5	50.0	223±5
6	93.3	216±5
7	116.7	231±6
8	78.1	229±8
9	87.5	223±6
Mean	–	224±6

3.5. Effects of heat treatment on microstructure and mechanical properties

3.5.1. Microstructural evolution after heat treatment

To evaluate the influence of post-processing treatments on the Ti-10Ta-2Nb-2Zr alloy, samples produced under optimal L-PBF conditions (Regime 3) were subjected to vacuum

annealing at 900°C for 1 h, followed by furnace cooling. This temperature was selected based on the DSC analysis results (Section 3.2), which identified a β-transus finish temperature of 862°C, ensuring complete transformation to the β-phase during the annealing process. The annealing temperature of 900°C was chosen to be approximately 40°C above the measured β-transus to guarantee complete transformation while minimizing grain growth.

The microstructural evolution resulting from heat treatment is illustrated in Figure 9, which presents SEM micrographs at different magnifications of the alloy after heat treatment.

As evident in Figure 9A, the heat treatment resulted in complete recrystallization of the as-built microstructure, with elimination of the directional features and melt pool boundaries that were characteristic of the L-PBF process. The previous fine acicular martensitic structure has been transformed into a well-defined lamellar arrangement of α + β phases. The microstructure exhibits a classical Widmanstätten or "basket-weave" pattern consisting of α-plates within prior β grains.

At higher magnification (Figure 9B), the structure reveals colonies of parallel α-plates, significantly coarser than the fine martensitic features observed in the as-built condition. The α-plates are arranged in multiple crystallographic orientations within individual prior β grains, which exhibit sizes of approximately 50 – 200 μm. Thin regions of retained β-phase are present between the α-plates, creating the characteristic lamellar structure.

The observed microstructural transformation can be attributed to the following mechanism: during heating above the β-transus temperature (862°C), the martensitic α' structure completely transforms to a single-phase β structure; subsequently, during the slow furnace cooling, α-phase nucleates preferentially at prior β grain boundaries and grows into the grains as parallel plates along specific crystallographic planes of the parent β-phase.

3.5.2. Phase composition changes

XRD analysis was performed to confirm the phase transformation resulting from heat treatment. Figure 7 presents a comparison of the XRD patterns for the as-built and heat-treated conditions.

The XRD pattern of the heat-treated alloy reveals significant differences compared to the as-built condition. While the as-built sample exhibited predominantly α' martensitic phase with peak broadening characteristic of high internal stresses, the heat-treated sample shows distinct peaks corresponding to both α and β phases. The presence of β-phase peaks, most notably at $2\theta \approx 38 - 39°$ (110) β, confirms the formation of a dual-phase structure during heat treatment.

In addition, the α-phase peaks in the heat-treated condition appear sharper and more defined compared to the as-built condition, indicating reduced internal stresses and increased crystallinity resulting from the annealing process. The peak positions also show slight shifts, reflecting compositional redistribution between α and β phases during the controlled cooling process.

3.5.3. Effects on mechanical properties

The microstructural evolution resulting from heat treatment had a significant impact on the mechanical properties of

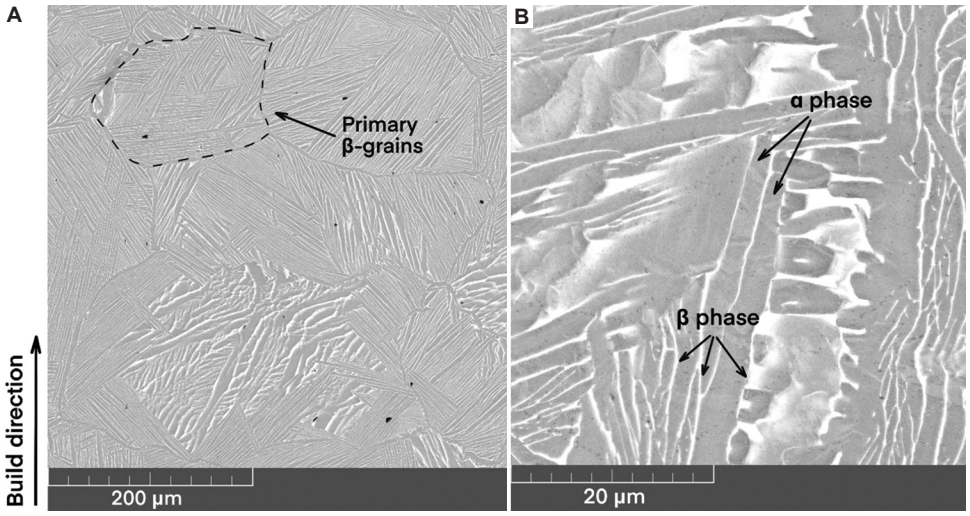

Figure 9. Scanning electron micrographs of Ti-10Ta-2Nb-2Zr alloy after heat treatment (vacuum annealing at 900°C for 1 h, furnace cooled). (A) Low magnification shows complete recrystallization and elimination of L-PBF-induced directional features, scale bar: 200 μm; magnification: ×500; (B) Higher magnification revealing characteristic lamellar α + β microstructure, scale bar: 20 μm; magnification: ×5000

the Ti-10Ta-2Nb-2Zr alloy. Table 3 summarizes the tensile properties before and after heat treatment.

The heat treatment had a significant impact on the mechanical properties of the Ti-10Ta-2Nb-2Zr alloy, as previously presented in Section 3.4. Heat treatment resulted in a notable reduction in strength properties, with yield strength decreasing from 551.8 ± 8.4 MPa to 452.3 ± 14.7 MPa (approximately 18% reduction) and ultimate tensile strength decreasing from 641.2 ± 5.7 MPa to 545.0 ± 3.6 MPa (approximately 15% reduction).

Heat treatment resulted in a notable reduction in strength properties, with yield strength decreasing by 18.0% and ultimate tensile strength by 15.0%. This strength reduction is directly attributable to the replacement of the fine martensitic structure with a coarser lamellar $\alpha + \beta$ microstructure, which offers fewer barriers to dislocation movement.

Interestingly, the elastic modulus decreased slightly from 89.0 GPa to 86.0 GPa (−3.4%) after heat treatment. This reduction, while modest, is beneficial for biomedical applications as it brings the material's stiffness closer to that of bone, potentially reducing stress-shielding effects in orthopedic implants.

The effect on ductility parameters was mixed: elongation increased from 19.0% to 20.2% (+6.3%), indicating improved uniform deformation capacity, while reduction in area decreased from 58.0% to 45.8% (−21.0%), suggesting a reduced localized necking ability. The greater variability in ductility measurements after heat treatment (standard deviations of 3.6% for elongation and 15.5% for reduction in area) indicates less consistent fracture behavior compared to the as-built condition.

The stress-strain curves confirm the reduced strength and slightly enhanced elongation after heat treatment (Figure 8). The heat-treated sample exhibits a more gradual transition from elastic to plastic deformation compared to the sharper yield point of the as-built condition, consistent with the more homogeneous, recrystallized microstructure with reduced internal stresses.

3.6. TPMS structures

Figure 10 presents experimental cylindrical specimens (6 mm diameter, 12 mm height) with different types of TPMS architectures fabricated using L-PBF with Ti-10Ta-2Nb-2Zr alloy. (A) Schwarz structure, (B) gyroid structure, and (C) split structure. All samples are characterized by 50% volumetric porosity and 1.5 mm unit cell size. The manufacturing quality of all structures confirms the technological capabilities of the L-PBF process for reproducing complex biomimetic architectures.

3.6.1. Compression mechanical properties

The results of compressive testing of Ti-10Ta-2Nb-2Zr lattice structures (Table 5) report characteristic features determined by their architecture and L-PBF process. The elastic modulus of all investigated lattice structures lies within a narrow range of 9.2 – 9.7 GPa, which represents approximately 18% of the solid material value (52.2 GPa). Such a significant reduction in stiffness is typical for porous structures and is attributed to the decreased volume fraction of material in the lattice.

The yield strength of lattice structures varies depending on their topology: the Schwarz structure shows the highest values (207.9 MPa), followed by gyroid (198.4 MPa) and split (193.6 MPa). These differences may be associated with the specific stress distribution patterns in different lattice topologies under compression.

Notably, the gyroid structure demonstrates the lowest scatter of experimental data among all investigated lattice types. The standard deviation is 2 – 3 times smaller compared to other structures (Figure 11). Such high reproducibility of results is attributed to the geometric

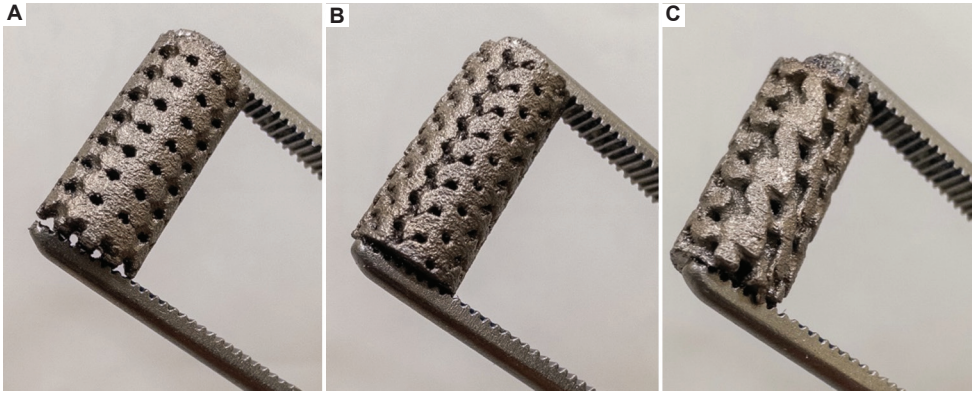

Figure 10. As-built cylindrical specimens with different types of triply periodic minimal surface. (A) Schwarz; (B) Gyroid; (C) Split

features of the gyroid lattice. The gyroid represents a triply periodic minimal surface with constant mean curvature, which provides the most uniform material distribution in space and eliminates sharp angles or abrupt cross-sectional changes characteristic of other topologies. This leads to more stable heat transfer conditions during the L-PBF process, minimization of stress concentrators, and consequently, enhanced reproducibility of mechanical properties among different specimens.

Table 5. Compression mechanical properties of lattice and solid structures

Structure	Elastic modulus (GPa)	Yield strength (MPa)
Schwarz	9.2±1.1	207.9±4.8
Gyroid	9.2±0.5	198.4±2.1
Split	9.7±0.4	193.6±5.9
Solid	52.2±8.4	539.3±23.3

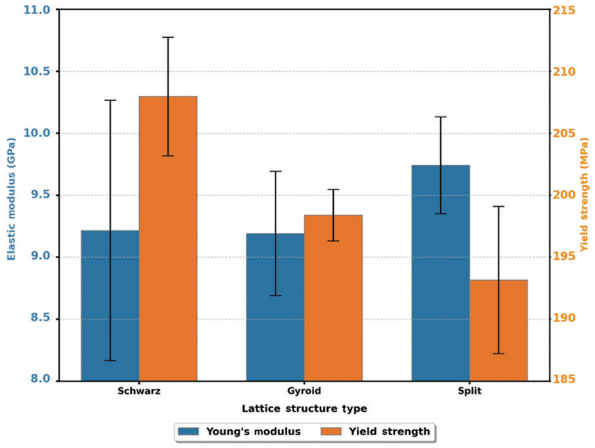

Figure 11. Compression mechanical properties of lattice structures

3.6.2. Triply periodic minimal surface microstructure analysis

Microstructural analysis of the etched surface of the gyroid structure revealed a characteristic microstructural gradient from the periphery to the center of lattice elements (Figure 12). The observed transition from fine acicular structure at the edges to coarser lamellar structure in the central regions reflects differences in crystallization conditions during L-PBF. Peripheral regions in contact with pores are characterized by higher cooling rates due to efficient heat dissipation through the gaseous medium and surrounding powder, which leads to the formation of fine acicular α'-martensitic structure. In the central regions of lattice elements, where heat dissipation is less intensive, slower cooling occurs, promoting the growth of coarser α' plates.

The observed microstructural gradient in TPMS struts reflects the complex thermal conditions during L-PBF processing of thin structural elements. Peripheral regions experience higher cooling rates due to efficient heat dissipation through the surrounding pore space and

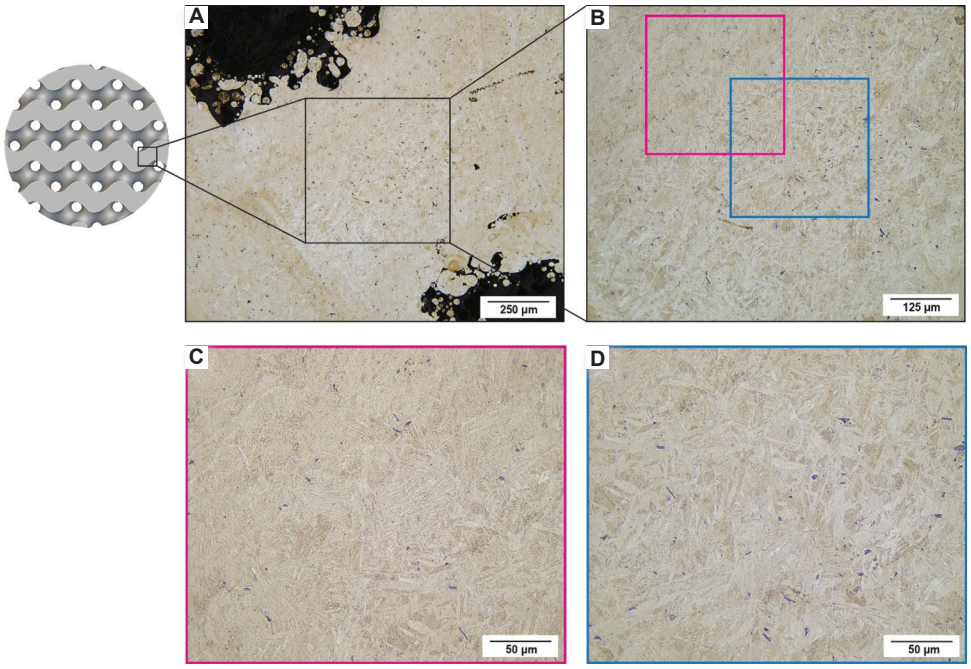

Figure 12. Optical microscope images of a gyroid-type structure. (A) AAA, scale bar: 250 µm; magnification: ×10; (B) BBB, scale bar: 250 µm; magnification: ×20; (C) CCC, scale bar: 50 µm; magnification: ×50; (D) DDD, scale bar: 50 µm; magnification: ×50

powder bed, resulting in finer microstructural features, while central regions undergo slower cooling due to thermal mass effects, producing coarser microstructural elements. This thermal gradient creates variations in residual stress distribution, phase constitution, and dislocation density throughout the strut cross-section. However, the mechanical behavior of lattice structures is governed by the overall microstructural homogeneity achieved through optimized L-PBF parameters rather than local microstructural variations. The consistent yield strength values of 194 – 208 MPa across different TPMS types demonstrate that the Ti-10Ta-2Nb-2Zr alloy maintains stable mechanical properties regardless of local thermal gradients. The excellent reproducibility observed, particularly in gyroid structures, indicates that the microstructural quality achieved through the optimized processing window ensures reliable mechanical performance of complex geometries.

4. Conclusion

A comprehensive investigation of Ti-10Ta-2Nb-2Zr alloy fabricated using L-PBF enabled the establishment of optimal processing regimes and characterization of structural-phase state and mechanical properties for biomedical applications.

(i) Systematic variation of L-PBF parameters revealed an optimal processing window: Laser power 250 – 280 W, scanning speed 600 – 800 mm/s, corresponding to volumetric energy density of 62.5 – 93.3 J/mm^3. Within this range, a maximum relative density of 99.91% was achieved, ensuring high mechanical integrity of components. Exceeding these energy parameters leads to keyhole porosity formation, reducing material density.

(ii) Microstructural analysis showed the formation of predominantly martensitic α'-phase in the as-built condition with characteristic acicular morphology due to high cooling rates during L-PBF. DSC determined β-transus temperature at 862°C. Heat treatment at 900°C provides complete recrystallization with the formation of equilibrium lamellar α + β structure, confirmed by XRD analyses.

(iii) Mechanical properties of Ti-10Ta-2Nb-2Zr alloy in as-built condition are characterized by high strength characteristics: yield strength 551.8 MPa, ultimate tensile strength 641.2 MPa, with elongation of 19.0% and elastic modulus of 89.0 GPa. Heat treatment reduces strength properties by 15 – 18% but decreases elastic modulus to 86.0 GPa, bringing it closer to the properties of bone tissue.

(iv) Developed porous structures based on TPMS (gyroid, Schwarz, and split) with 50% volumetric porosity demonstrate an elastic modulus of 9.2 – 9.7 GPa, representing approximately 18% of the solid material value. Among the investigated topologies, the gyroid structure showed the best reproducibility of mechanical properties due to uniform stress distribution. Microstructural analysis of porous elements revealed a gradient from fine acicular structure at the periphery to coarser lamellar structure in central regions, providing an optimal combination of strength and ductility.

The obtained results confirm the high potential of the Ti-10Ta-2Nb-2Zr alloy for the additive manufacturing of orthopedic implants using the L-PBF process.

Acknowledgments

None.

Funding

This research was supported by the Ministry of Science and Higher Education of the Russian Federation (agreement No. 075-15-2024-562).

Conflicts of interest

The authors declare they have no competing interests.

Author contributions

Conceptualization: Igor Polozov, Anatoly Popovich
Formal analysis: Igor Polozov, Victoria Nefyodova, Anton Zolotarev
Investigation: Igor Polozov, Anton Zolotarev, Victoria Nefyodova
Methodology: Igor Polozov, Anatoly Popovich
Project administration: Igor Polozov
Resources: Anatoly Popovich
Supervision: Anatoly Popovich
Writing – original draft: Igor Polozov
Writing – review & editing: Anatoly Popovich, Victoria Nefyodova

Ethics approval and consent to participate

Not applicable.

Consent for publication

Not applicable.

Availability of data

The datasets used and/or analyzed during the current study are available from the corresponding author on reasonable request. Raw data files for mechanical testing, microstructural analysis, and selective laser melting

processing parameters can be obtained by contacting the corresponding author.

References

1. Wu H, Chen X, Kong L, Liu P. Mechanical and biological properties of Ti and its alloys for oral implant with preparation techniques: A review. *Materials (Basel)*. 2023;16(21):6860.

   doi: 10.3390/ma16216860

2. Khorasani AM, Goldberg M, Doeven EH, Littlefair G. Titanium in biomedical applications-properties and fabrication: A review. *J Biomater Tissue Eng*. 2015;5(8):593-619.

   doi: 10.1166/jbt.2015.1361

3. Zhang Y, Xiu P, Jia Z, *et al*. Effect of vanadium released from micro-arc oxidized porous Ti6Al4V on biocompatibility in orthopedic applications. *Colloids Surf B Biointerfaces*. 2018;169:366-374.

   doi: 10.1016/j.colsurfb.2018.05.044

4. Abdel-Hady Gepreel M, Niinomi M. Biocompatibility of Ti-alloys for long-term implantation. *J Mech Behav Biomed Mater*. 2013;20:407-415.

   doi: 10.1016/j.jmbbm.2012.11.014

5. Laheurte P, Prima F, Eberhardt A, Gloriant T, Wary M, Patoor E. Mechanical properties of low modulus β titanium alloys designed from the electronic approach. *J Mech Behav Biomed Mater*. 2010;3(8):565-573.

   doi: 10.1016/j.jmbbm.2010.07.001

6. Han L, Che S. An overview of materials with triply periodic minimal surfaces and related geometry: From biological structures to self-assembled systems. *Adv Mater*. 2018;30(17):e1705708.

   doi: 10.1002/adma.201705708

7. Learmonth ID, Young C, Rorabeck C. The operation of the century: Total hip replacement. *Lancet*. 2007;370(9597):1508-1519.

   doi: 10.1016/S0140-6736(07)60457-7

8. khan B, Kumar S. *Implementation of Triply Periodic Minimal Surface (TPMS) Structure in Mesenchymal Stem Cell Differentiation*. United States: Research Square; 2022.

   doi: 10.21203/rs.3.rs-2156625/v1

9. Castro APG, Pires T, Santos JE, Gouveia BP, Fernandes PR. Permeability versus design in TPMS scaffolds. *Materials (Basel)*. 2019;12(8):1313.

   doi: 10.3390/ma12081313

10. Chen LY, Cui YW, Zhang LC. Recent development in beta titanium alloys for biomedical applications. *Metals (Basel)*. 2020;10(9):1139.

    doi: 10.3390/met10091139

11. Niinomi M, Boehlert CJ. Titanium alloys for biomedical applications. In: *Advances in Metallic Biometerials*. Berlin: Springer; 2015. p. 179-213.

    doi: 10.1007/978-3-662-46836-4_8

12. Bahl S, Suwas S, Chatterjee K. Comprehensive review on alloy design, processing, and performance of β Titanium alloys as biomedical materials. *Int Mater Rev*. 2021;66(2):114-139.

    doi: 10.1080/09506608.2020.1735829

13. Niinomi M. Mechanical biocompatibilities of titanium alloys for biomedical applications. *J Mech Behav Biomed Mater*. 2008;1(1):30-42.

    doi: 10.1016/j.jmbbm.2007.07.001

14. Huang S, Sing SL, De Looze G, Wilson R, Yeong WY. Laser powder bed fusion of titanium-tantalum alloys: Compositions and designs for biomedical applications. *J Mech Behav Biomed Mater*. 2020;108:103775.

    doi: 10.1016/j.jmbbm.2020.103775

15. Fuerst J, Medlin D, Carter M, Sears J, Vander Voort G. LASER additive manufacturing of titanium-tantalum alloy structured interfaces for modular orthopedic devices. *JOM*. 2015;67(4):775-780.

    doi: 10.1007/s11837-015-1345-4

16. Sing SL, Yeong WY, Wiria FE. Selective laser melting of titanium alloy with 50 wt% tantalum: Microstructure and mechanical properties. *J Alloys Compd*. 2016;660:461-470.

    doi: 10.1016/j.jallcom.2015.11.141

17. Plaine AH, Silva MR, Bolfarini C. Effect of thermo-mechanical treatments on the microstructure and mechanical properties of the metastable β-type Ti-35Nb-7Zr-5Ta alloy. *Mater Res*. 2018;22(1):e20180462.

    doi: 10.1590/1980-5373-mr-2018-0462

18. Ummethala R, Karamched PS, Rathinavelu S, *et al*. Selective laser melting of high-strength, low-modulus Ti–35Nb–7Zr–5Ta alloy. *Materialia*. 2020;14:100941.

    doi: 10.1016/j.mtla.2020.100941

19. Zhang LC, Klemm D, Eckert J, Hao YL, Sercombe TB. Manufacture by selective laser melting and mechanical behavior of a biomedical Ti-24Nb-4Zr-8Sn alloy. *Scrip Mater*. 2011;65(1):21-24.

    doi: 10.1016/j.scriptamat.2011.03.024

20. Hao YL, Yang R, Niinomi M, *et al*. Young's modulus and mechanical properties of Ti-29Nb-13Ta-4.6Zr in relation to α" martensite. *Metall Mater Trans A*. 2002;33(10):3137-3144.

    doi: 10.1007/s11661-002-0299-7

21. Yang K, Wang J, Tang H, Li Y. Additive manufacturing of in-situ reinforced Ti-35Nb-5Ta-7Zr (TNTZ) alloy by selective electron beam melting (SEBM). *J Alloys Compd*. 2020;826:154178.

doi: 10.1016/j.jallcom.2020.154178

22. Brodie EG, Medvedev AE, Frith JE, Dargusch MS, Fraser HL, Molotnikov A. Remelt processing and microstructure of selective laser melted Ti25Ta. *J Alloys Compd*. 2020;820:153082.

doi: 10.1016/j.jallcom.2019.153082

23. Ji G, Zhou Z, Meng F, *et al*. Effect of Zr addition on the local structure and mechanical properties of Ti-Ta-Nb-Zr refractory high-entropy alloys. *J Mater Res Technol*. 2022;19:4428-4438.

doi: 10.1016/j.jmrt.2022.06.160

24. Biesiekierski A, Lin J, Li Y, Ping D, Yamabe-Mitarai Y, Wen C. Investigations into Ti-(Nb,Ta)-Fe alloys for biomedical applications. *Acta Biomater*. 2016;32:336-347.

doi: 10.1016/j.actbio.2015.12.010

25. Zhenhuan W, Yu D, Junsi L, *et al*. Physiochemical and biological evaluation of SLM-manufactured Ti-10Ta-2Nb-2Zr alloy for biomedical implant applications. *Biomed Mater*. 2020;15(4):045017.

doi: 10.1088/1748-605X/ab7ff4

26. Morita A, Fukui H, Tadano H, Hayashi S, Hasegawa J, Niinomi M. Alloying titanium and tantalum by cold crucible levitation melting (CCLM) furnace. *Mater Sci Eng A*. 2000;280(1):208-213.

doi: 10.1016/S0921-5093(99)00668-1

27. Zhao D, Han C, Li Y, *et al*. Improvement on mechanical properties and corrosion resistance of titanium-tantalum alloys *in-situ* fabricated via selective laser melting. *J Alloys Compd*. 2019;804:288-298.

doi: 10.1016/j.jallcom.2019.06.307

28. Soro N, Brodie EG, Abdal-hay A, Alali AQ, Kent D, Dargusch MS. Additive manufacturing of biomimetic titanium-tantalum lattices for biomedical implant applications. *Mater Des*. 2022;218:110688.

doi: 10.1016/j.matdes.2022.110688

29. Yoo DJ. Computer-aided porous scaffold design for tissue engineering using triply periodic minimal surfaces. *Int J Precis Eng Manuf*. 2011;12(1):61-71.

doi: 10.1007/s12541-011-0008-9

30. Yoo DJ. Porous scaffold design using the distance field and triply periodic minimal surface models. *Biomaterials*. 2011;32(31):7741-7754.

doi: 10.1016/j.biomaterials.2011.07.019

31. Dilip JJS, Zhang S, Teng C, *et al*. Influence of processing parameters on the evolution of melt pool, porosity, and microstructures in Ti-6Al-4V alloy parts fabricated by selective laser melting. *Prog Addit Manuf*. 2017;2(3):157-167.

doi: 10.1007/s40964-017-0030-2

32. Xiang S, Yuan Y, Zhang C, Chen J. Effects of process parameters on the corrosion resistance and biocompatibility of Ti6Al4V parts fabricated by selective laser melting. *ACS Omega*. 2022;7(7):5954-5961.

doi: 10.1021/acsomega.1c06246

33. Pesode P, Barve S. A review-metastable β titanium alloy for biomedical applications. *J Eng Appl Sci*. 2023;70(1):25.

doi: 10.1186/s44147-023-00196-7

34. Liu CC, Li YHZ, Gu J, Song M. Phase transformation in titanium alloys: A review. *Trans Nonferrous Metals Soc China*. 2024;34(10):3093-3117.

doi: 10.1016/S1003-6326(24)66597-0

35. Banerjee D, Williams JC. Perspectives on titanium science and technology. *Acta Mater*. 2013;61(3):844-879.

doi: 10.1016/j.actamat.2012.10.043

36. Ahmed T, Rack HJ. Phase transformations during cooling in α+β titanium alloys. *Mater Sci Eng A*. 1998;243(1-2):206-211.

doi: 10.1016/S0921-5093(97)00802-2

37. Bania PJ. Beta titanium alloys and their role in the titanium industry. *JOM*. 1994;46(7):16-19.

doi: 10.1007/BF03220742

38. Geetha M, Singh AK, Asokamani R, Gogia AK. Ti based biomaterials, the ultimate choice for orthopaedic implants - A review. *Prog Mater Sci*. 2009;54(3):397-425.

doi: 10.1016/j.pmatsci.2008.06.004

39. Jamshidi P, Aristizabal M, Kong W, *et al*. Selective laser melting of Ti-6Al-4V: The impact of post-processing on the tensile, fatigue and biological properties for medical implant applications. *Materials*. 2020;13(12):2813.

doi: 10.3390/ma13122813

40. Cho JY, Xu W, Brandt M, Qian M. Selective laser melting-fabricated Ti-6Al-4V alloy: Microstructural inhomogeneity, consequent variations in elastic modulus and implications. *Opt Laser Technol*. 2019;111:664-670.

doi: 10.1016/j.optlastec.2018.08.052